Apatite germanates doped with tungsten: synthesis, structure, and conductivity

A. Orera[1], T. Baikie[2], E. Kendrick[3], J.F. Shin[6], S. Pramana[1], R. Smith[4], T. J. White[5], M.L. Sanjuán[1], and P.R. Slater[6*]

[1] Instituto de Ciencia de Materiales de Aragón, C.S.I.C.-Universidad de Zaragoza, E-50.009 Zaragoza, Spain

[2]Nanyang Technological University, School of Materials Science and Engineering, 50 Nanyang Avenue, 639798, Singapore.

[3]Chemical Sciences, University of Surrey, Guildford, Surrey, GU2 7XH, UK

[4]ISIS Facility, Rutherford Appleton Laboratory, Harwell Science and Innovation Campus, Didcot, OX11 0QX. UK

[5] Centre for Advanced Microscopy, Australian National University, Canberra, ACT 2601 Australia

[6]School of Chemistry, University of Birmingham, Birmingham. B15 2TT. UK

[*]Correspondence to:

Dr. P.R. Slater

School of Chemistry, University of Birmingham, Birmingham. B15 2TT. UK

Tel. +44 (0)121 4148906

Fax +44 (0) 121 414403

p.r.slater@bham.ac.uk

Abstract

High oxygen content apatite germanates, $La_{10}Ge_{6-x}W_xO_{27+x}$, have been prepared by doping on the Ge site with W. In addition to increasing the oxygen content, this doping strategy is shown to result in stabilisation of the hexagonal lattice, and yield high conductivities. Structural studies of $La_{10}Ge_{5.5}W_{0.5}O_{27.5}$ show that the interstitial oxygen sites are associated to a different degree with the Ge/WO_4 tetrahedra, leading to five coordinate Ge/W and significant disorder for the oxygen sites associated with these units. Raman spectroscopy studies suggest that in the case of the WO_5 units, the interstitial oxygen is more tightly bonded and therefore not as mobile as in the case of the GeO_5 units, thus not contributing significantly to the conduction process.

1. Introduction

Apatite-type materials, ideal general formula $A_{10}M_6O_{24}X_2$ (A=alkaline earth, rare earth; M=P, Si, Ge; X=OH, O, halide), have been widely researched, with applications ranging from biomaterials to ionic conductors. Notionally, their crystal structure can be described as a $A_4(MO_4)_6$ framework, with the remaining A_6X_2 units accommodated in the channels, formed by the framework (figure 1). In terms of applications as ionic conductors, the silicates/germanates, $La_{9.33+2x/3}(Si/Ge)_6O_{26+x}$ have been shown to represent a new class of oxide ion conductor, with potential use in solid oxide fuel cells [1-40]. A key feature of these apatite oxide ion conductors is that their conduction mechanism is driven by the presence of interstitial oxide ions, contrary to the traditional fluorite and perovskite systems, where oxide ion vacancies are responsible [13]. For the silicates it has been shown that oxygen excess in the range, $0 \leq x \leq 0.5$ is possible, while higher oxygen content, $0 \leq x \leq 1.0$ has been achieved for the germanates [13, 18, 20, 21]. For the silicate series, the exact location of extrastoichiometric oxygen, x, has attracted some controversy, with reports of interstitial sites close to the SiO_4 tetrahedra, while in other studies, mobile oxygen at the centre of the channels has been claimed [4, 8, 9, 10, 12, 13, 23, 27, 35, 36]. For the germanates, the situation appears more clearcut, with computer modeling, neutron diffraction and Raman studies indicating occupancy by oxygen sites close to the GeO_4 tetrahedra leading to the formation of five coordinate Ge [10, 20-22, 37, 40].

A considerable amount of work has been performed on doping studies in the silicate apatites, as summarized in the review article by our group [13]. In contrast, there have been fewer doping studies performed on the germanate systems, despite the fact that these systems can accommodate higher oxygen interstitial contents, important for high oxide ion conductivity in apatite systems [13]. The important role of interstitial

oxygen has been demonstrated by recent work on the germanate apatite series, $La_{8+2x}Ba_{2-2x}Ge_6O_{26+x}$, where conductivity increases with x for $0 \leq x \leq 0.7$. However, for $x > 0.7$, the apatite symmetry is reduced from hexagonal to triclinic, with a coincident depression of conductivity at low temperatures that is attributed to more efficient trapping of the interstitial oxygen [24]. The same transition to a triclinic cell is observed for the $La_{9.33+2x/3}Ge_6O_{26+x}$ series at high values of x [7,10, 20, 21]. Therefore it is important to identify strategies to maintain hexagonal symmetry at high oxide ion contents to maintain high conductivities.

The triclinic distortion has been attributed to a size mismatch between the $La_{3.33+2x/3}(GeO_4)_6$ framework and the La_6O_2 channels leading to underbonding at the channel La atoms, which is relieved by the triclinic distortion, through twisting of the GeO_4 tetrahedra [20,21,39]. In prior work, we have shown that Y can be selectively doped into the La sites within the $La_{3.33+2x/3}(GeO_4)_6$ framework altering the diameter, and hence relieving the triclinic distortion [18, 37]. In this way it is possible to prepare hexagonal samples with high oxygen content, i.e. $La_{7.33+2x/3}Y_2(GeO_4)_6O_{2+x}$ ($0 \square x \square 1.0$), which show enhanced conductivity at low temperatures compared with equivalent triclinic samples without Y doping [18]. We have also investigated the effect of doping the lower valent Co^{3+}, Ga^{3+} ions on the Ge site, $La_{10}Ge_{6-x}(Co/Ga)_xO_{27-x/2}$, although in these cases the dopant appears to enhance the triclinic distortion [13, 19]. This can be explained by the dopants enlarging the framework, and hence exacerbating the underbonding at the channel La sites, and driving the triclinic distortion.

Recently we have extended this Ge site doping work to investigate doping higher valent ions on the Ge sites, and here we report the successful incorporation of W into $La_{10}Ge_6O_{27}$. Through W doping it is shown that the stabilization of the hexagonal cell is achieved, while the higher valence of W means that the total oxygen content is

increased above 27, which represents the highest oxygen content reported for these systems. The crystal structure and location of the interstitial oxide ions in $La_{10}Ge_{5.5}W_{0.5}O_{27.5}$ have been determined through neutron diffraction and Raman spectroscopy studies, while the conductivity was measured by AC impedance spectroscopy.

2. Experimental

Stoichiometric amounts of high purity La_2O_3, GeO_2, and WO_3 were ground together, and heated for 12 hours at 1100ºC, with a second firing at 1100ºC for a further 12 hours. Between firings the samples were reground to ensure homogeneity. The samples were subsequently ball milled for 1 hour (350 rpm, Fritsch Pulverisette 7 Planetary Mill), before heating at 1300°C for 2 hours. Phase purity was established through X-ray powder diffraction (Bruker D8 diffractometer with Cu $K\alpha_1$ radiation).

Conventional sintering of these W doped apatite systems for conductivity measurements led to undesirable low density compacts (≈60% theoretical). To overcome this problem, spark plasma sintering (SPS) was carried out at the *Plateforme Nationale de Frittage Flash/CNRS* [1] at Toulouse, France. In this process, 1 g of sample was pressed in a 15.4mm diameter graphite die at 100MPa and 1200°C. The maximum pressure and temperature were maintained for less than 2 minutes, followed by the fast release of the pressure and natural cooling of the samples. The residual carbon was burnt off the pellets by heating at 950°C for several hours before coating both sides with platinum paste for conductivity measurements.

Conductivity measurements were made on the pellets (≈85% theoretical) using AC impedance spectroscopy (Hewlett Packard 4182A impedance analyser) in the range

[1]PNF2/CNRS – MHT, Université Paul Sabatier, Toulouse, France. Created by P. Millet, P. Rozier, J. Galy, 2003-2004.

from 0.1 to 10^3 kHz. The collected impedance data were analysed using equivalent circuits to separate both bulk and grain boundary contributions to the resistance (see supplementary information for representative plots).

Time of flight powder neutron diffraction data were collected on the POLARIS diffractometer at the ISIS pulsed spallation source, Rutherford Appleton Laboratory, UK. Structure refinement was then carried out with the GSAS suite of Rietveld refinement software, using data collected in the highest resolution backscattering detector bank ($<2\theta>=145^{\circ}$) [41].

Raman spectroscopy measurements were carried out using a backscattering setup with an optical microprobe spectrometer (Model XY, Dilor, France) with a CCD detector. Room temperature spectra were taken through a X 50 microscope objective lens in a 4 microns diameter sample region. The power of the laser line was 40mW and the spectral resolution ~2 cm^{-1}. High temperature spectra were taken with a LINKAM TS1500 stage with a temperature stability of 0.5K, and using a X50 long working distance objective lens. The 514.5 nm line of an Ar^+-ion laser (Model INNOVA 305, Coherent, Palo Alto, CA) was used for sample excitation and the Si Raman line at 520 cm^{-1} for wavelength calibration.

3. Results and Discussion

X-ray diffraction studies, on the samples prepared, indicated that it was possible to prepare W doped germanates, $La_{10}Ge_{6-x}W_xO_{27+x}$, in the range $0 \leq x \leq 0.5$. At the highest dopant concentration, x=0.5, the sample was hexagonal, while at low levels, the samples were triclinic as for the undoped phase (figure 2).

Impedance measurements showed that for the low W content triclinic phases (x=0.1), the conductivity at low temperatures was rather low, consistent with the expected

defect trapping in the triclinic cell. In contrast, the conductivity for $La_{10}Ge_{5.5}W_{0.5}O_{27.5}$, which was hexagonal, was significantly higher at low temperature (figure 3). Both compositions showed similar conductivities at high temperature, as they both exhibit hexagonal symmetry at these elevated temperatures (high temperature X-ray diffraction data showed that for $La_{10}Ge_{5.9}W_{0.1}O_{27.1}$, there is a triclinic-hexagonal phase transition between 700 and 750°C). The similar high temperature conductivities ($\sigma \approx 0.02$ S cm^{-1} at 820°C) of the x=0.1, and 0.5 samples is interesting, and suggests that either there is an upper limit for the magnitude of the oxide ion conductivity with increasing oxygen content, such that there is an optimum oxygen interstitial concentration, or there could be partial trapping of the interstitial oxide ion defects by W, which counterbalances the effect of the increase in oxygen content.

Following our recent work on the study of the position and mobility of interstitial oxygen in the apatite germanates, $La_{8+x}Ba_{2-x}Ge_6O_{26+x/2}$ by Raman spectroscopy, we performed Raman dispersion measurements on samples with different W content. Figure 4 shows the Raman spectra of $La_{10}Ge_{5.7}W_{0.3}O_{27.3}$ and $La_{10}Ge_{5.5}W_{0.5}O_{27.5}$. These spectra are very similar to those of $La_{8+x}Ba_{2-x}Ge_6O_{26+x/2}$ [40]. In particular, they present the band at ~ 645 cm^{-1} whose intensity was correlated with interstitial oxygen content in Ref [40]. However, an additional band at 830 cm^{-1} is observed in the W-doped samples, its intensity increasing with W content. No other band is found at higher frequencies, up to at least 1200 cm^{-1}. According to Hardcastle et al [42], this frequency (830 cm^{-1}) is much lower than that expected for the stretching of a W-O bond in an ideal WO_4 tetrahedron, suggesting a higher coordination of tungsten in the form of WO_5 or even WO_6. These results imply the distribution of the interstitial oxygen between both germanium and tungsten. In fact, from the line-shape analysis of these spectra, the intensity of the 645 cm^{-1} band, attributed to the presence of

interstitial oxide ions resulting in the formation of five coordinate Ge, remains constant with increasing W content. That means that the extra oxygen ions introduced by the aliovalent doping with hexavalent W do not form GeO_5 units, but increase the coordination of the dopant. In order to study the effect of this interstitial site on the ionic conductivity, we have performed high temperature Raman measurements on the $La_{10}Ge_{5.5}W_{0.5}O_{27.5}$ sample. Figure 5 shows the Raman spectra of this sample at temperatures ranging from RT to 700ºC. These spectra have been corrected by dividing by the prefactor (n(ω,T)+1) affecting the Raman intensities, where n(ω,T) is the Bose-Einstein factor, n(ω,T)=1/(exp(ħω/kT)-1). Apart from the expected broadening of the Raman bands, the only change observed is the thermally activated decrease in the intensity and subsequent disappearance of the 645 cm^{-1} band that was attributed to the "freeing" of the interstitial oxide ions from the GeO_5 units and hence the onset of significant oxide ion conduction [40]. No intensity decrease is observed for the 830 cm^{-1} band (see supplementary information), suggesting that the tungsten groups are not significantly involved in the conduction process. This fact would explain the similar high temperature conductivity values measured for $La_{10}Ge_{5.5}W_{0.5}O_{27.5}$ and $La_{10}Ge_{5.9}W_{0.1}O_{27.1}$ (figure 3) and even $La_8Y_2Ge_6O_{27}$ [44], regardless the different oxygen content. The beneficial effect of W doping on the low temperature oxide ion conductivity of these apatite systems would then merely lie in the stabilization of the hexagonal phase.

As there have been recent reports of water incorporation in apatite germanates [16, 43], the conductivity measurements were repeated under a wet atmosphere. These data showed no change in the bulk conductivities, although for $La_{10}Ge_{5.5}W_{0.5}O_{27.5}$ there was a slight enhancement of the grain boundary conductivity (figure 6). The change from H_2O hydrated nitrogen gas to D_2O-hydrated led to a slight decrease in

this enhancement, suggesting the presence of an isotopic effect and hence suggesting that the increase in this grain boundary conductivity was due to a protonic contribution.

The structure of the highly conducting hexagonal sample, $La_{10}Ge_{5.5}W_{0.5}O_{27.5}$, was then analysed in detail using powder neutron diffraction measurements. In the refinement, space group $P6_3/m$, which is typical for apatite systems, was employed. The initial structural model employed the non-electroneutral cell ($La_{10}Ge_{5.5}W_{0.5}O_{26}$) containing no interstitial oxide ions. Fourier maps showed the presence of unfitted nuclear density between two Ge/WO_4 units, at a position close to (0,0.5,0.5), while for the channel oxygen sites (0,0,0.25), a large spread of nuclear density along the z direction was observed, consistent with a large degree of static disorder. In addition, these Fourier maps suggested significant disorder within the oxide-ion sites of the Ge/WO_4 tetrahedra, in particular the O3 site (see supplementary information). In order to account for these features, extra oxygen was placed on the interstitial site between the tetrahedra, while the O3 site was split, with the atomic displacement parameters of the split sites constrained as equal, while their occupancies were linked such that the total occupancy (O3a + O3b) =1.0. Similar features were observed in the refinement of the related high oxygen content hexagonal apatite germanate, $La_8Y_2Ge_6O_{27}$, and in modelling studies on $La_{9.33}Ge_6O_{26}$ [22, 37]. The latter indicated that the presence of interstitial oxide ions, leading to the formation of "GeO_5" units, results in substantial displacement of the other oxygens on the original GeO_4 unit [22]. Due to the high correlation between the atomic displacement parameter and the site occupancy factor for the interstitial site, the occupancy was fixed at that expected from the sample stoichiometry. For the channel oxide ion, O4, the ion was allowed to move off the mirror plane at z= ¼ , ¾, leading to two closely spaced sites, each with

half occupancy. The same off-site displacement was also allowed for the O2 site of the tetrahedra. The final structural data are given in table 1, and the neutron diffraction profiles and structural figure shown in supplementary information. Selected bond distances are given in table 2, which show that the refined model overall gives sensible bond distances. It should, however, be noted that the data in table 2b does show some apparently short (<2.5Å) O-O distances. However, these split oxygen sites are not fully occupied, and therefore occupancy of both sites in close proximity can be eliminated through local oxygen ordering.

Further improvements in the fit could be made by introducing more disorder of the oxide ion sites, but in these cases the refinement led to some unreasonably short Ge/W-O bond distances. Similarly a refinement without split sites, but with anisotropic atomic displacement parameters was also examined. Although this gave slightly smaller 'R' values, it also gave some physically unreasonable values for the atomic displacement parameters (see supplementary information), while we believe that the split site model provides a realistic interpretation of the local distortions. Overall the results suggest that although the long range structure is hexagonal, there is considerable local disorder, such that the local structure may be more likely triclinic, as for the undoped system. Indeed the diffuse background in the ND profiles (supplementary information) suggests significant short range correlations, most likely to eliminate short O-O interactions, consistent with the observed high atomic displacement parameters and need for split oxide ion sites. This emphasises the complexity of these apatite systems, and suggests the need for further total scattering experiments to investigate these short range features.

As with the structure refinements for related $La_{10}Ge_6O_{27}$ and $La_8Y_2Ge_6O_{27}$ [20,21, 37], the neutron diffraction data showed the presence of interstitial oxide ions

between the tetrahedra. This position gives physically sensible Ge/W-O bond distances, and is also in agreement with predictions made by modelling studies [22] and results from the Raman studies discussed earlier. With respect to the latter, by collecting data from many W oxides, Hardcastle et al. [42] proposed an exponential functional form that relates the W-O bond distance to the frequency of the W-O stretching vibration. Using that relation for a frequency 830 cm^{-1} we obtain d(W-O) ≈1.81 Å, which is slightly larger than the average Ge/W-O distance derived from neutron diffraction, in agreement with the larger size of W compared to Ge. From the powder neutron diffraction data collected in this study, it is not possible to determine whether the interstitial oxide ions are spread randomly over all available O5 positions in the crystal, or whether they associate preferentially with framework tetrahedral sites containing W (or alternatively Ge). However, as detailed earlier the Raman results suggest that two kinds of interstitial oxide ions exist: those introduced by W doping appear to be tightly bound to W atoms, forming WO5 entities, whereas interstitial oxygen ions close to GeO4 tetrahedra, forming GeO5 units, are loosely bound and release easily upon heating.

The occupancy of the interstitial oxide ion site also leads to significant displacements in the other oxygen sites of the tetrahedra as well as the channel oxygen site, as indicated by the high atomic displacement parameters, and the need for split sites for O3, as well as displacement of the O2 and O4 oxide ions off-site. The presence of W on the Ge site is also likely to be contributing to the local disorder.

An interesting further feature to explain is why the presence of a higher valent dopant, W, stabilises the hexagonal lattice, since it is known that high oxygen excess leads to triclinic cells. Calculation of the metaprism twist angle gives a value of 24.9°, which is on the borderline of what would be expected for a hexagonal cell, indicating that

the composition is at the hexagonal-triclinic barrier limit, consistent with lower W dopant levels giving triclinic cells, as well as the large local disorder implied by the neutron diffraction study.

The origin of this triclinic distortion has been shown to be a result of lattice mismatch between the framework and the channels, with the presence of interstitial oxide ions within the framework increasing this mismatch leading to a tilting of the tetrahedra and hence a triclinic cell. In this case, W^{6+} is not only slightly larger than Ge^{4+}, but it also increases the oxygen content, both features expected to enhance the triclinic distortion, not to reduce it. A similar stabilisation of the hexagonal lattice has been observed after doping with Ti, or Nb [44], whereas work on doping with lower valent ions, e.g. Co or Ga, has shown that increasing the size of the tetrahedral cation leads to a greater triclinic distortion [13, 19]. Thus $La_{10}Ge_4Ga_2O_{26}$ is triclinic, even though it has nominally no oxygen excess [19]. This anomaly clearly needs more study, although it is suggested that it may be related to interstitial defect trapping by the dopant leading to the formation of MO_5 units and consequent local relief of lattice strain by the dopant. The Raman studies, reported here, show clear evidence for this defect trapping in the case of W, while such defect trapping has also been inferred from conductivity studies for the series $La_{10}Ge_{6-x}Ti_xO_{27}$ [44].

4. Conclusions

In summary, we have successfully doped W into the apatite system $La_{10}Ge_6O_{27}$ leading to an increase in symmetry from triclinic (undoped phase) to hexagonal for $La_{10}Ge_{5.5}W_{0.5}O_{27.5}$, and a corresponding increase in the low temperature conductivity. The interstitial oxide ion sites are confirmed to be located within the framework in between two isolated tetrahedra, leading to the formation of five coordinate Ge/W.

Moreover Raman spectroscopy suggests that some of the interstitial oxide ions are trapped as WO_5 and do no participate significantly in the conduction process.

Acknowledgements

We would like to express thanks to EPSRC for funding (grant EP/F015178/2) and the Science and Technology Facilities Council (STFC) for the provision of neutron diffraction beam time at the ISIS facility. We would also like to acknowledge funding through A*STAR SERC Grant 082 101 0021 "*Optimization of Apatite Anion Sublattices in Solid Oxide Fuel Cell Electrolytes*". Financial support from Spanish project MAT2007-64486-C07-02 is also acknowledged.

The Bruker D8 diffractometer used in this research was obtained through the Science City Advanced Materials project: Creating and Characterising Next generation Advanced Materials project, with support from Advantage West Midlands (AWM) and part funded by the European Regional Development Fund (ERDF).

References

1. S. Nakayama, H. Aono, Y. Sadaoka, *Chem. Lett.* (1995) 431.

2. S. Nakayama, M. Sakamoto, M. Higuchi, K. Kodaira, *J. Mater. Sci. Lett*. 19 (2000) 91.

3. S. Tao, J.T.S. Irvine, *Mater. Res. Bull.* 36 (2001) 1245.

4. J.E.H. Sansom, D. Richings, P.R. Slater, *Solid State Ionics* 139 (2001) 205.

5. H. Arikawa, H. Nishiguchi, T. Ishihara, Y. Takita, *Solid State Ionics* 136-137 (2000) 31.

6. L. Leon-Reina, M.E. Martin-Sedeno, E.R. Losilla, A. Caberza, M. Martinez-Lara, S. Bruque, F.M.B. Marques, D.V. Sheptvakov, M.A.G. Aranda; *Chem. Mater*. 15 (2003) 2099.

7. E.J. Abram, C.A. Kirk, D.C. Sinclair, A.R. West; *Solid State Ionics* 176 (2005) 1941.

8. J. R. Tolchard, P. R. Slater, M. S. Islam; Adv. Funct. Mater. 17 (2007) 2564.

9. J.R. Tolchard, M.S. Islam, P.R. Slater; *J. Mater. Chem*. 13 (2003) 1956; A. Jones, P.R. Slater, M.S. Islam; Chem Mater 20 (2008) 5055.

10. L. Leon-Reina, E.R. Losilla, M. Martinez-Lara, M.C. Martin-Sedeno, S. Bruque, P.Nunez, D.V. Sheptyakov, M.A.G. Aranda; *Chem. Mater*. 17 (2005) 596; L. Leon-Reina, E.R. Losilla, M. Martinez-Lara, S. Bruque, A. Llobet, D.V. Sheptyakov, M.A.G. Aranda; *J. Mater. Chem.* 15 (2005) 2489.

11. V.V. Kharton, A.L. Shaula, M.V. Patrakeev, J.C. Waerenborgh, D.P. Rojas, N.P. Vyshatko, E.V. Tsipis, A.A. Yaremchenko, F.M.B. Marques; *J. Electrochem. Soc*. 151 (2004) A1236.

12. J.E.H. Sansom, J.R. Tolchard, D. Apperley, M.S. Islam, P.R. Slater; *J. Mater. Chem.* 16 (2006) 1410.

13. E. Kendrick, M.S. Islam, P.R. Slater; *J. Mater. Chem*. 17 (2007) 3104.

14. Y. Masubuchi, M. Higuchi, S. Kikkawa, K. Kodaira, S. Nakayama; *Solid State Ionics* 175 (2004**)** 357.

15. S. Celerier, C. Laberty-Robert, J.W. Long, K.A. Pettigrew, R.M. Stroud, D.R. Rolison, F. Ansart, P. Stevens, *Adv. Mater*. 18 (2006**)** 615.

16. L. Leon-Reina, J.M. Porras-Vasquez, E.R. Losilla, M.A.G. Aranda; *J. Solid State Chem.* 180 (2007) 1250.

17. E. Kendrick, J.R.Tolchard, J.E.H. Sansom, M.S. Islam, P.R. Slater; *Faraday Discussions* 134 (2007) 181.

18. E. Kendrick, P.R. Slater; *Mater. Res. Bull*. 43 (2008) 2509.

19. E. Kendrick, P.R. Slater; *Mater. Res. Bull*. 43 (2008) 3627.

20. S. S. Pramana, W.T. Klooster and T. J. White; *Acta Cryst*. B 63 (2007) 597.

21. S.S. Pramana, W.T. Klooster, T.J. White; *J. Solid State Chem*. 181 (2008) 1717.

22. E. Kendrick, M.S. Islam, P.R. Slater; *Chem. Commun*. (2008) 715.

23. A. Orera, E. Kendrick, D. C. Apperley, V.M. Orera, P.R. Slater; *Dalton Trans*. (2008) 5296.

24. E. Kendrick, P.R. Slater; *Solid State Ionics* 179 (2008) 981.

25. P.J. Panteix, I. Julien, P. Abelard, D. Bernache-Assolant; *Ceram. Int*. 34 (2008) 1579.

26. T. Iwata, K. Fukuda, E. Bechade, O. Masson, I. Julien, E. Champion, P. Thomas; *Solid State Ionics* 178 (2008) 1523.

27. R. Ali, M. Yashima, Y. Matsushita, H. Yoshioka, K. Okoyama, F. Izumi; *Chem. Mater.* 20 (2008) 5203.

28. J.R. Tolchard, P.R. Slater; *J. Phys. Chem. Solids* 69 (2008) 2433.

29. E. Kendrick, P.R. Slater; *Mater. Res. Bull*. 43 (2008) 3627.

30. A. Orera, P.R. Slater; *Solid State Ionics* (2009); doi 10.1016/j.ssi.2008.12.014

31. E. Kendrick, K.S. Knight, P.R. Slater; *Mater. Res. Bull*. 44 (2009) 1806.

32. J.M. Porras-Vazquez, E.R. Losilla, L. Leon-Reina, D. Marrero-Lopez, M.A.G. Aranda; *J. Am. Ceram. Soc*. 92 (2009) 1062.

33. C. Bonhomme, S. Beaudet-Savignat, T. Chartier, P-M. Geffroy, A-L. Sauvet ; *J. Euro. Ceram. Soc.* 29 (2009) 1781.

34. A. Al-Yasari, A. Jones, D.C. Apperley, D. Driscoll, M.S. Islam, P.R. Slater; *J. Mater. Chem.* 19 (2009) 5003.

35. E. Bechade, O. Masson, T. Iwata, I. Julien, K. Fukuda, P. Thomas, E. Champion; *Chem. Mater*. 21 (2009) 2508.

36. S. Guillot, S. Beaudet-Savignat, S. Lambert, R-N. Vannier, P. Roussel, F. Porcher; J. Solid State Chem. 182 (2009) 3358.

37. E. Kendrick, A. Orera, P.R. Slater; *J. Mater. Chem.* 19, (2009) 7955.

38. A. Orera, D. Headspith, D.C. Apperley, M.G. Francesconi, P.R. Slater; *J. Solid State Chem.* 182 (2009) 3294.

39. T.J. White and Z.L. Dong; *Acta Crystallogr*. B 59 (2003) 1.

40. A. Orera, M. L. Sanjuán, E. Kendrick, V. M. Orera, P.R. Slater; *J. Mater. Chem*. 20, (2010) 2170.

41. A.C. Larson, R.B. Von Dreele. *Los Alamos National Laboratory, Report*. No LA-UR-86-748 (1987).

42. F.D. Hardcastle, I.E. Wachs; *J. Raman Spectrosc*. 26 (1995) 397-405.

43. A. Orera, P.R. Slater; *Solid State Ionics* 181 (2010) 110.

44. A. Orera, T. Baikie, P. Panchmatia, T.J. White, J. Hanna, M.E. Smith, M.S. Islam, P.R. Slater; Fuel Cells (in press).

Table 1. Refined crystal structure data for $La_{10}Ge_{5.5}W_{0.5}O_{27.5}$ from neutron TOF data.

S.G.	$P6_3/m$	a = 9.9302(2) Å	c = 7.3159(2) Å	wR_p = 0.0304	R_P = 0.0404
				wR_{exp} = 0.0079	R_F = 0.084
Site	***x***	***y***	***z***	**100 × U_{Iso}**	**Occ.**
La(1)	1/3	2/3	0.0023(5)	2.42 (6)	1.0
La(2)	0.2316(3)	-0.0100(3)	0.25	1.38(4)	1.0
Ge/W	0.4007(2)	0.3764(2)	0.25	0.92(3)	0.9167/0.0833
O(1)	0.3062(4)	0.4838(3)	0.25	2.95*	1.0
O(2)	0.6038(3)	0.4695(3)	0.2789(5)	0.67(7)	0.5
O(3a)	0.3587(4)	0.2566(3)	0.0633(4)	1.92(6)	0.672(4)
O(3b)	0.2731(6)	0.2338(7)	0.0942(7)	1.91(5)	0.328(4)
O(4)	0	0	0.207 (1)	4.5(3)	0.5
O(5)	0.034(1)	0.496(2)	0.519(2)	3.6(2)	0.125

*

	U_{11}	U_{22}	U_{33}	U_{12}	U_{13}	U_{23}
O(1)	4.7(2)	2.3(2)	2.7(2)	2.4(2)	0	0

Table 2. Selected interatomic distances and angles

(a)

Bond	**Distance (Å)**
La(1)-O(1)	2.483(3)
La(1)-O(2)	2.394(4), 2.701(5)
La(1)-O(3a)	2.799(4)
La(1)-O(5)	2.59(1)
La(2)-O(1)	2.714(4)
La(2)-O(2)	2.580(3)
La(2)-O(3a)	2.526(3), 2.669(3)
La(2)-O(3b)	2.516(7), 2.536(5)
La(2)-O(4)	2.372(2)
***B*-O(1)**	1.738(3)
***B*-O(2)**	1.765(3)
***B*-O(3a)**	1.720(3)
***B*-O(3b)**	1.765(5)
***B*-O(5)**	1.92(2)

(b)

Bond	**Distance (Å)**
O(5) – O(1)	2.620(15), 2.639(14)
O(5) – O(2)	2.165(14), 2.281(14), 2.621(12), 1.805(15)
O(5) – O(3a)	1.829(13), 2.494(13),

O(5) – O(3b)	2.307(13), 2.853(11)

(c)

Angle	°
O(1)-*B*-O(3a)	113.9(2)
O(1)-*B*-O(2)	120.4(2)
O(2)-*B*-O(3a)	106.1(2), 95.0(2)
O(3a)-*B*-O(3a)	105.1(2)

(d)

Angle	°
O(1)-*B*-O(3b)	95.8(2)
O(1)-*B*-O(5)	91.6(4)
O(1)-*B*-O(2)	120.4(2)
O(2)-*B*-O(3b)	121.2(2), 132.3(3)
O(2)-*B*-O(5)	58.5(4), 71.9(4)
O(3b)-*B*-O(3b)	80.4(4)
O(3b)-B-O(5)	157.4(4)

***B* = Ge/W**

Figure Captions

Figure 1. The Apatite structure $A_{10}M_6O_{24}X_2$, in terms of an $A_4(MO_4)_6$ framework composed of face sharing AO_6 trigonal meta-prismatic columns, that are corner connected to the MO_4 tetrahedra. The remaining A_6X_2 units occupy the "cavities".

Figure 2. X-ray diffraction patterns for $La_{10}Ge_{5.9}W_{0.1}O_{27.1}$ (bottom, triclinic cell) and $La_{10}Ge_{5.5}W_{0.5}O_{27.5}$ (top, hexagonal cell). The former shows peak broadening/splitting arising from the lower symmetry cell.

Figure 3. Bulk conductivity data for $La_{10}Ge_{5.9}W_{0.1}O_{27.1}$ and $La_{10}Ge_{5.5}W_{0.5}O_{27.5}$ showing an enhancement in the conductivities at temperatures <700°C for the latter.

Figure 4. Raman spectra of $La_{10}Ge_{5.7}W_{0.3}O_{27.3}$ and $La_{10}Ge_{5.5}W_{0.5}O_{27.5}$.

Figure 5. High temperature Raman spectra of $La_{10}Ge_{5.5}W_{0.5}O_{27.5}$. The spectra are divided by the Bose factor (n+1)

Figure 6. Grain Boundary conductivity data for $La_{10}Ge_{5.5}W_{0.5}O_{27.5}$ under dry and wet N_2 showing a small enhancement for the latter.

Figure 1

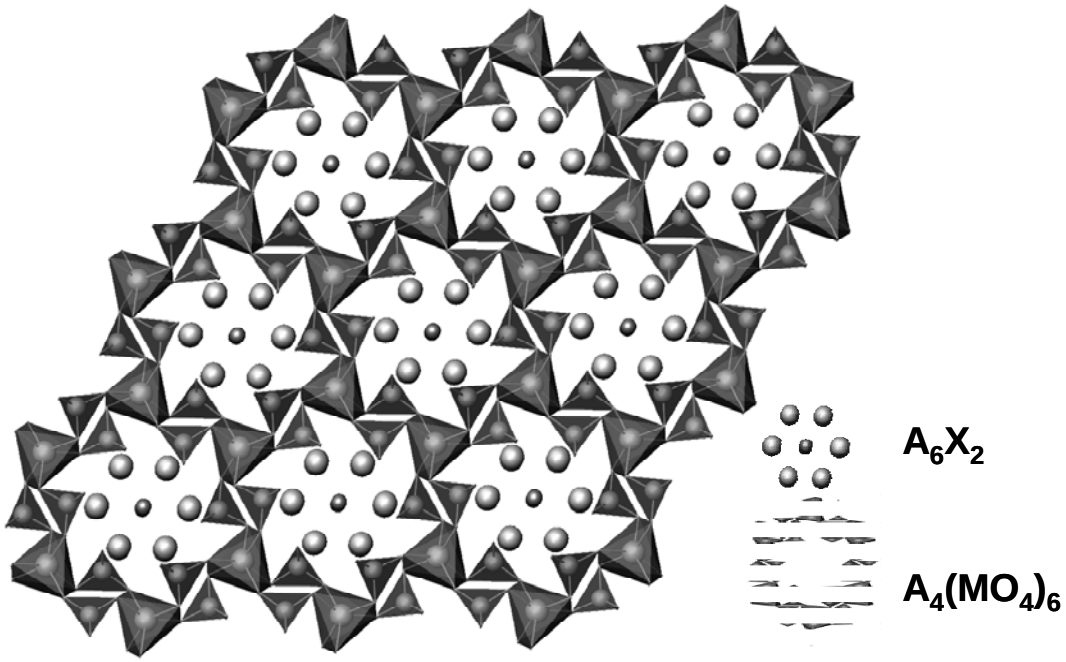

Figure 2.

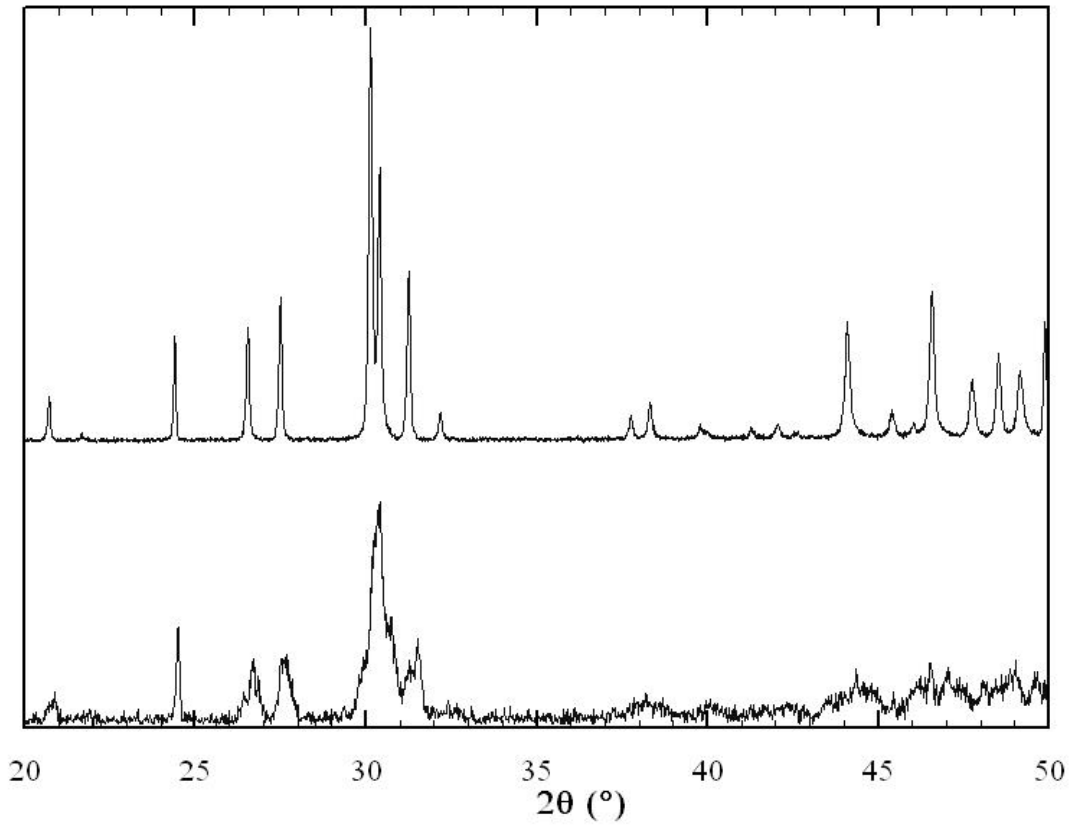

Figure 3

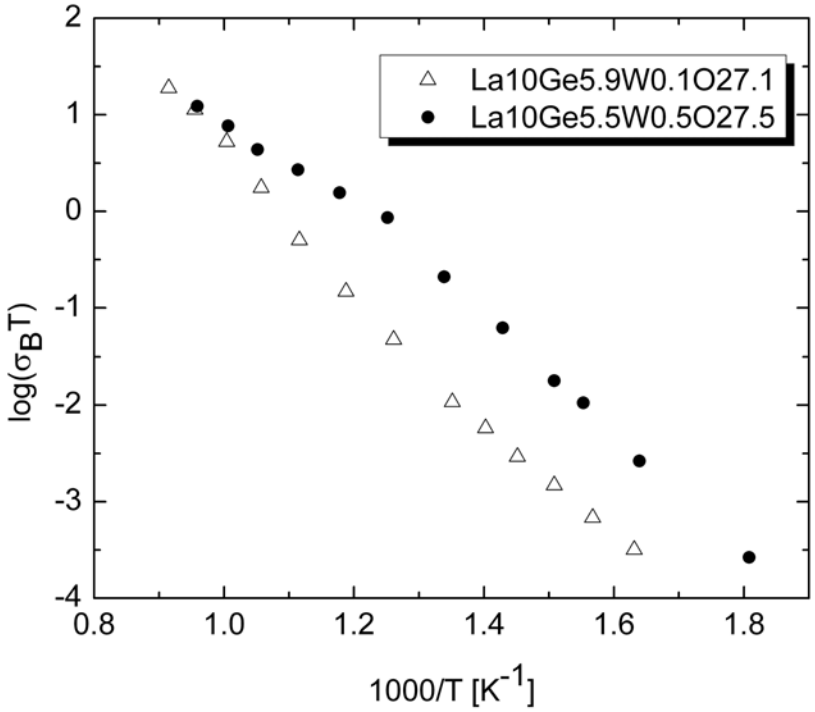
La10Ge5.9W0.1O27.1
La10Ge5.5W0.5O27.5
log(σBT)
1000/T [K-1]
2
1
0
-1
-2
-3
-4
0.8
1.0
1.2
1.4
1.6
1.8

Figure 4

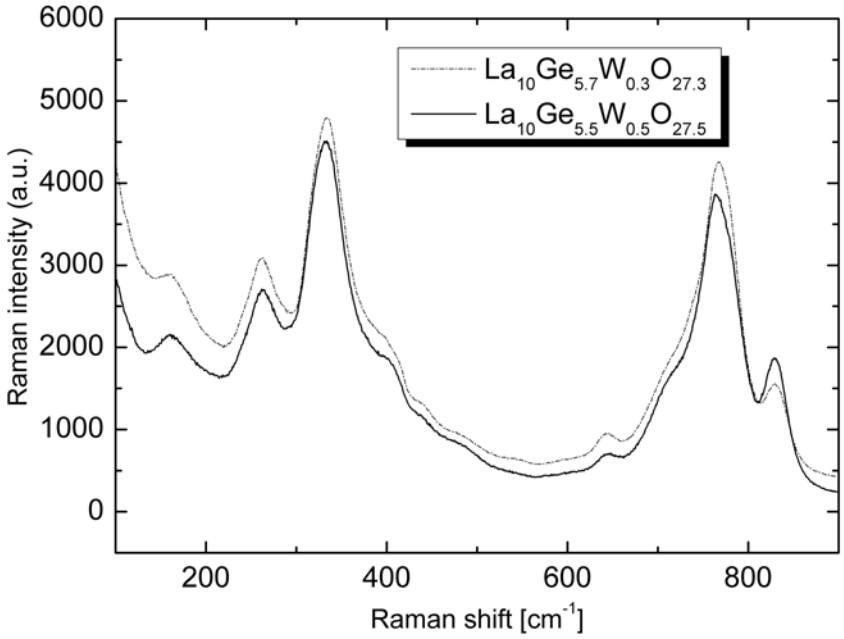
6000
5000
4000
3000
2000
1000
0
Raman intensity (a.u.)
200
400
600
800
Raman shift [cm-1]
La10Ge5.7W0.3O27.3
La10Ge5.5W0.5O27.5

Figure 5

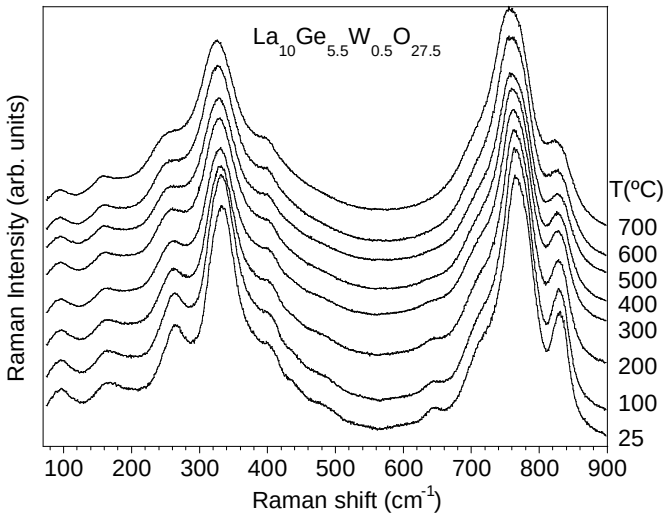
La10Ge5.5W0.5O27.5
Raman Intensity (arb. units)
T(ºC)
700
600
500
400
300
200
100
25
100
200
300
400
500
600
700
800
900
Raman shift (cm-1)

Figure 6.